HHS Public Access

Author manuscript

AIDS. Author manuscript; available in PMC 2022 September 01.

Published in final edited form as:

AIDS. 2021 September 01; 35(11): 1733–1741. doi:10.1097/QAD.0000000000002960.

Chemical exchange saturation transfer for detection of antiretroviral drugs in brain tissue

Aditya N. BADE[1], **Howard E. GENDELMAN**[1], **JoEllyn MCMILLAN**[1], **Yutong LIU**[1,2,‡]

[1]Department of Pharmacology and Experimental Neuroscience, University of Nebraska Medical Center, Omaha, NE 68198 USA

[2]Department of Radiology, University of Nebraska Medical Center, Omaha, NE 68198 USA

Abstract

Objective: Antiretroviral drug (ARV) theranostics facilitates the monitoring of biodistribution and efficacy of therapies designed to target human immunodeficiency virus type-1 (HIV-1) reservoirs. To this end, we have now deployed intrinsic drug chemical exchange saturation transfer (CEST) contrasts to detect ARVs within the central nervous system (CNS).

Design and Methods: CEST effects for lamivudine (3TC) and emtricitabine (FTC) were measured by asymmetric magnetization transfer ratio analyses. The biodistribution of 3TC in different brain sub-regions of C57BL/6 mice treated with lipopolysaccharides was determined using magnetic resonance imaging (MRI). CEST effects of 3TC protons were quantitated by Lorentzian fitting analysis. 3TC levels in plasma and brain regions were measured using ultraperformance liquid chromatography tandem mass spectrometry to affirm the CEST test results.

Results: CEST effects of the hydroxyl and amino protons in 3TC and FTC linearly correlated to drug concentrations. 3TC was successfully detected *in vivo* in brain sub-regions by MRI. The imaging results were validated by measurements of CNS drug concentrations.

Conclusion: CEST contrasts can be used to detect ARVs using MRI. Such detection can be used to assess spatial-temporal drug biodistribution. This is most notable within the CNS where drug biodistribution may be more limited with the final goal of better understanding ARV-associated efficacy and potential toxicity.

‡Corresponding Author: Yutong Liu, Associate Professor, Department of Radiology, ESH 1020C, University of Nebraska Medical Center, Omaha, NE 68198-1045; yutongliu@unmc.edu; phone: (402)559-8340.

Author contributions

A.N.B.: designed the study, performed antiretroviral and animals experiments, collected and analyzed data, and wrote and edited the manuscript.

H.E.G.: provided guidance in study design and manuscript writing-editing.

J.M.M.: analyzed UPLC/MS-MS data sets.

Y.L.: conceived project and central hypothesis, designed the study, developed scientific approach for CEST MRI data acquisition and analysis methods, collected, analyzed and interpreted data sets, and wrote and edited the manuscript.

All authors critically evaluated the manuscript prior to submission.

Conflicts of Interest: Dr. Howard E. Gendelman is Co-founder of Exavir Therapeutics, Inc., a biotechnology company focused on the development of long acting antiretroviral medicines. For the remaining authors none were declared.

Keywords

CEST; Theranostics; HIV-1; 3TC; Antiretroviral

Introduction

Although antiretroviral therapy (ART) can prolong the life of human immunodeficiency virus type-1 (HIV-1) infected patients[1–4], neurocognitive disorders persist and occur in up to 50% of infected patients[5, 6]. Disease ranges from asymptomatic neurocognitive impairment (ANI) to mild neurocognitive disorder (MND) and to the most severe form HIV-associated dementia (HAD) [6]. Persistent viral replication in the central nervous system (CNS) elicits neuroimmune activation and is associated with cognitive decline [5, 7, 8]. Thus, it is imperative to begin ART early after infection to slow disease progression and attenuate mental health deficits that are associated with advanced disease [9–13]. ART can be a double edge sword by reversing cognitive decline while in select instances speeding adverse clinical outcomes [14, 15]. The latter include neuropsychiatric, motor and behavioral events [16, 17]. Therefore, the ability to follow drug pharmacokinetics (PK) and biodistribution (BD) could serve as a powerful tool to suppress or perhaps limit the establishment of viral CNS reservoirs and minimize off-target ART effects within the CNS.

Chemical exchange saturation transfer (CEST) as a contrast mechanism was employed previously for drug detection [21]. It arises when an exchangeable proton of a macromolecule is magnetically saturated and transferred to water by chemical exchange causing water MRI signal reduction that reflects macromolecule concentrations. Continuous proton exchanges between the macromolecule and water leading to the buildup of the signal reduction, and the large number of water molecules in tissue amplify detection [18–22]. Compared to traditional drug detection systems that tag medicines with an imaging agent or load drugs and imaging agents into a nanoparticle, CEST-based imaging does not require extrinsic imaging agents. This eliminates the limitations associated with therapeutic efficacy by reduced loading capacity [23] and toxicity [24, 25]. Herein, we developed HIV theranostics based on the CEST contrasts of ARVs. CEST effects of nucleoside reverse transcriptase inhibitors (NRTIs) including lamivudine (3TC) and emtricitabine (FTC) were characterized. Proof-of-concept for CEST-based ARV theranostics was developed for 3TC and drug biodistribution in brain sub-regions of mice was traced using MRI.

Materials and Methods

Study approvals

All animal studies were approved by the University of Nebraska Medical Center Institutional Animal Care and Use Committee (IACUC) in accordance with the standards incorporated in the Guide for the Care and Use of Laboratory Animals (National Research Council of the National Academies, 2011).

Reagents

Lamivudine (3TC) was purchased from BOC Sciences (Shirley, NY). Emtricitabine (FTC) was purchased from HBCChem (Union City, CA). (Hydroxypropyl)methyl cellulose (HPMC), polysorbate 80 (TWEEN® 80), and lipopolysaccharide (LPS) were purchased from Sigma-Aldrich (St. Louis, MO). Gibco™ DPBS, LC-MS grade water and methanol were purchased from Fisher Scientific (Waltham, MA). 0.9% Sodium Chloride Injection, USP was purchased from Hospira (Lake Forest, IL).

CEST contrasts of 3TC and FTC

CEST contrasts of 3TC and FTC were measured in phosphate buffered saline (PBS) at 37 °C on a 7 Tesla scanner (Bruker PharmaScan 70/16, Billerica, MA) using a Bruker quadrature RF coil. CEST data were acquired using a Rapid Imaging with Refocused Echoes (RARE) sequence with TR/TE = 4000/42 ms, RARE factor = 16, saturation RF power = 3.6 μT, and duration = 3 s. To construct Z-spectra, saturation frequencies were set from −8 to +8 ppm, step = 0.2 ppm. A second RARE data with saturation RF power = 0.5 μT, and frequencies = −1 to +1 ppm were acquired for B0 correction using WASSR [26]. An image of RF power = 0 μT was acquired as baseline (S_0) for the normalization of CEST images. Following B0 correction and normalization, Z-spectra were constructed. A Z-spectrum is the water signal as a function of saturation frequency, and asymmetric magnetism transfer ratio (MTR_{asym}) was calculated from the Z-spectrum:

$$MTR_{asym} = \frac{S(-\Delta\omega) - S(+\Delta\omega)}{S(-\Delta\omega)} \quad [1]$$

where $\Delta\omega$ is the frequency offset between the saturation frequency and the water frequency (0 ppm), and $S(-\Delta\omega)$ and $S(+\Delta\omega)$ are the water signal intensities at the offset frequency lower than water (upfield) and higher than water (downfield), respectively.

3TC administration to mice

Male C57BL/6 mice (14 – 16 weeks old) were purchased from the Jackson Laboratory (Bar Harbor, ME). Mice were randomly distributed in two groups, control and 3TC-treated. First, to mimic the inflammatory response of HIV-1 infected patients, mice from both groups (3TC and control) were administered daily 1 mg/kg of LPS by intraperitoneal injection in 100 μL sterile saline [27–29] for five days, starting at 24 hours before the first dose of 3TC. The last dose (5th dose) of LPS was administered at 24 hours before MRI at day 5. Second, 3TC solution prepared in a vehicle (0.2% hydroxypropylmethyl cellulose and 0.1% Tween 80 in sterile water) was administered to mice (3TC group) daily by oral gavage for 5 days at a dose of 250 mg/kg. Six hours post-final 3TC dose administration at day 5, mice were scanned for CEST imaging. Control mice were given vehicle alone.

Animal CEST MRI

CEST imaging was performed on controls (n = 8) and 3TC-treated mice (n = 7) on a 7 Tesla MRI scanner (Bruker BioSpec 70/20, Billerica, MA). A Bruker-made volume quadrature RF coil was employed for signal transmission and a Bruker 4-element coil array was used for signal reception. Respiration and body temperature were monitored during scanning. CEST

data were acquired using a RARE sequence (TR/TE = 1600/16 ms, RARE factor = 8) with a continuous RF for saturation with the power = 2 μT, duration = 1 s, saturation frequencies = −5 to 5 ppm in steps of 0.2 ppm. A second CEST data with saturation RF power = 0.5 μT, and frequencies = −1 to +1 ppm were acquired for B0 inhomogeneity correction using WASSR [26]. An image of RF power = 0 μT was acquired as baseline (S_0) for the normalization of CEST images.

Based on the CEST effects of 3TC shown in Figure 1, the *in vivo* Z-spectra were first normalized using S_0 (baseline image of RF power = 0 μT) and then fitted using a five-pool Lorentzian model of bulk water, aliphatic nuclear Overhauser effect (NOE), magnetization transfer (MT) contrast, amide and amino CEST effects:

$$L_i(\Delta\omega) = \frac{A_i}{1 + 4\left(\frac{\Delta\omega - \omega_i}{\Gamma_i}\right)^2} \quad [2]$$

where $\Delta\omega$ is the saturation frequency related to water at 0 ppm; A_i, ω_i, and Γ_i are respectively the amplitude, chemical shift and full width at half maximum (FWHM) of the ith CEST peak. The initial values of A_i, ω_i, and Γ_I of NOE, amide and MT were set according to previous brain CEST studies [30–36]. The initial values of amino effect were set at ω = 2 ppm, Γ = 1.5 ppm based on the measurements of 3TC shown in Figure 1. A number of amplitudes (A = 0.05 ~ 0.2) were tried and the fitting results were similar. The integral under each Lorentzian line was calculated pixel by pixel.

PK and BD of 3TC in mice

3TC concentrations in plasma and brain tissue samples of 3TC-treated mice (n = 5) were measured by ultraperformance tandem mass spectrometry (UPLC-MS/MS) using a Waters ACQUITY H-class UPLC (Waters, Milford, MA) connected to a Xevo TQ-S micro mass spectrometer [37–39]. All solvents for sample processing and UPLC-MS/MS analysis were LC-MS-grade (Fisher Scientific). 3TC levels in plasma were measured at 6 hours and day 5 time points. Blood samples were collected into heparinized tubes by cheek puncture (submandibular vein) using a 5 mm lancet (MEDIpoint, Inc., Mineola, NY). Collected blood samples were centrifuged at 2,000 × g for 8 minutes to collect plasma. Plasma samples were stored at −80 °C for further quantitation of 3TC levels. At day 5 following MRI, animals were humanely euthanized; and brain regions (hippocampus, cortex, and mid-brain) were isolated for quantitation of 3TC concentrations. For plasma drug quantitation 25 µl of plasma was added to 1 ml of ice-cold acetonitrile. Tissue samples were weighed and homogenized in a solution of 90% methanol/10% water. 100 μL of each tissue homogenate was then added to 1 mL of ice-cold methanol. For plasma and tissue drug analysis, acetonitrile-precipitated plasma and methanol-precipitated brain tissue were vortexed for 3 minutes, followed by 10-minute centrifugation at 16000 × g. The resulting supernatant was collected into a new tube and dried down using a SpeedVac (Savant SPD1010, Thermo Scientific). Samples were reconstituted in 80% methanol and 3TC levels were quantitated using UPLC-MS/MS as described [37].

Statistics

Statistical analyses were conducted using GraphPad Prism 7.0 software (La Jolla, CA). Results from *in vivo* studies were expressed as mean ± standard error of the mean (SEM). Student's t tests were performed to compare *in vivo* CEST imaging results from the control and 3TC groups. Pearson's correlation was used to determine the association between 3TC imaging results and brain tissue drug levels measured by UPLC-MS/MS.

Results

CEST contrasts of 3TC and FTC

The CEST contrasts of 3TC and FTC are shown in Figure 1. 3TC is a cytidine analog, and its chemical structure includes a hydroxyl proton and an amino proton (Figure 1A). The CEST contrasts of these protons were assessed using 3TC solutions at 10, 20, 50, and 100 mM. The MTR_{asym} plots of 3TC and PBS are shown in Figure 1B. The CEST effects of the hydroxyl and amino protons were observed at 1 and 2 ppm on the MTR_{asym} plots. The CEST effects were increased with the concentration of 3TC. PBS did not show any CEST effect (Figure 1B). The CEST effect of the amino proton (at 2 ppm on MTR_{asym}) was linearly proportional to the 3TC concentration with a correlation coefficient $R^2 = 0.95$ (Figure 1C). The amino effects of 3TC samples are presented in heatmaps in Figure 1D. The color intensity increased with the concentration of 3TC. Concentration-dependent CEST analysis was also performed for the hydroxyl proton (at 1 ppm on MTR_{asym}). Similarly, the CEST effect of hydroxyl proton was linearly increased with 3TC concentration ($R^2 = 0.94$; Supplementary Figure S1A – B). Further, the CEST effects of cytidine analogs were validated using another ARV – FTC (Figure 1E to 1H). Similar to 3TC, concentration dependent CEST effects of the hydroxyl and amino protons of FTC (10, 20, 50 or 100 mM) were observed at 1 and 2.4 ppm, respectively, on the *MTRasym* plots (Figure 1F). However, the CEST effect of FTC amino proton shifted to 2.4 ppm and its magnitude was higher compared to 3TC (Figure 1B vs. Figure 1F). The CEST effect of the amino proton (at 2.4 ppm on MTR_{asym}) was linearly proportional to the FTC concentration with a correlation coefficient $R^2 = 0.90$ (Figure 1G). Increase in color intensity with FTC concentration compared to control (PBS) confirmed the CEST contrast generated by the amino group of FTC (Figure 1H). The CEST effect of the hydroxyl (at 1 ppm on MTR_{asym}) of FTC also linearly increased with the drug concentration ($R^2 = 0.89$; Supplementary Figure S1C – D).

CEST in 3TC-treated mice

CEST effects of 3TC were measured on brain sub-regions in C57BL/6 male mice following daily oral drug administration for 5 days at a dose of 250 mg/kg. This dose was about five times of human dosage after animal equivalent dose (AED) calculation [40]. Vehicle to dissolve 3TC was used as control to avoid any confounders. T_2-weighted images were used as an anatomical reference for brain region-of-interest (ROI) analysis (Figure 2A). The CEST 3TC effect was measured in five sub-regions of the CNS - hippocampus (HIP), cortex (CTX), piriform cortex (PIR), thalamus (TH) and hypothalamus (HY). The Z-spectra of brain regions were built from CEST MRI data. Figure 2B shows representative Z-spectra on HIP of a control and a 3TC-treated mouse. Z-spectra on other brain regions (CTX, TH, PIR, and HY) are shown in Supplementary Figure S2. In a Z-spectrum, the water proton signal

is plotted as a function of saturation frequency, and a CEST effect is represented as a signal drop on the Z-spectrum at certain saturation frequency. The evident signal drop from the direct saturation of the bulk water occurred at 0 ppm (Figure 2B). Signal drops at ~ 2 ppm and 3.5 ppm resulted from amino and amide protons, respectively (Figure 2B). The signal at 2 ppm in the 3TC mouse was larger than in the control mouse, indicating the CEST effect of the 3TC amino proton. The signal drop within −1.0 ~ −4.0 ppm resulted from aliphatic NOE (Figure 2B), which is a type of cross-relaxation pathway where spin polarization exchange takes place. A five-pool Lorentzian function was used to fit the bulk water, aliphatic NOE, MT, amino and amide protons. MT contrast is a broad, non-specific signal drop in the Z-spectrum from semi-solid macromolecules [31, 36, 41–44]. Representative fitting results in the control and the 3TC-treated mouse on HIP are shown in Figure 2C and 2D, respectively. The fitting results on CTX, PIR, TH and HY are demonstrated in Supplementary Figure S3. For better visualization, fitted bulk water and MT were removed and fitted functions of NOE, amino and amide protons are shown in Figure 2E and Supplementary Figure S3. Compared to the controls, increase (in both amplitude and linewidth) in amino proton effect (at about 2 ppm) was observed on all brain sub-regions of the 3TC group (Figure 2E and Supplementary Figure S3). The amide proton effects (at about 3.5 ppm) were comparable between the control and the 3TC groups (Figure 2E and Supplementary Figure S3). NOE was reduced in 3TC-treated mice compared to in controls. Pixel-by-pixel heatmaps of the integrals of the fitted amino Lorentzian line on brain sub-regions were shown in Figure 3A–3D. T_2-weighted images were used as an anatomical reference (Figure 3A and 3C). Higher color intensity of the amino CEST effect compared to controls is seen on all brain sub-regions of the 3TC group (Figure 3B and 3D). The 3TC group had a significant increase of amino CEST effect compared to the controls on CTX ($p = 0.028$), HIP ($p = 0.047$), TH ($p = 0.039$), PIR ($p = 0.044$) and HY ($p = 0.024$) (Figure 3E). No significant differences were found in amide effects between the control and 3TC groups (Supplementary Figure S4A – E). A trend of decrease was observed for NOE in 3TC mice on HIP ($p = 0.099$) and TH ($p = 0.082$) compared to controls (Supplementary Figure S4F – J). This change indicated that 3TC induced biochemical changes in brain.

Further, 3TC levels were measured in plasma and brain sub-regions using UPLC-MS/MS and were correlated to CEST MRI results (Figure 4A and 4B). An average of 1009 ± 154.6 ng/mL and 2819.1 ± 880.1 ng/mL of 3TC was measured in plasma at 6 hours and day 5, respectively. In addition, 3TC levels were 473.3 ± 199.6 ng/g in HIP, 532.6 ± 192 ng/g in CTX and 614.5 ± 227.2 ng/g in mid-brain at day 5. The correlation coefficients of 3TC CEST and UPLC-MS/MS data were $R^2 = 0.62$ on CTX, and $R^2 = 0.20$ on HIP (Figure 4C and 4D). The correlation of CEST contrasts on CTX and HIP together with 3TC levels in both regions was $R^2 = 0.37$ (Figure 4E).

Discussion

CEST contrasts of ARVs can be characterized and utilized for the measurement of biodistribution in brain sub-regions using MRI. In traditional theranostic technologies, drug molecules are tagged with imaging agents or loaded with imaging agents into one nanoparticle. Paramagnetic metals are commonly used for MRI [45–47] and radioactive materials used for positron emission tomography (PET) and single photon emission

computed tomography (SPECT) [48–51]. The limitations of the methods are obvious. First, the loading rate of nanoparticles are usually limited to achieve effective therapy and/or imaging sensitivity [23]. Second, toxicity associated with imaging agents and nanoparticles has to be addressed [52–54]. Third, blood brain barrier penetration needs to be considered when designing traditional theranostic methods for the CNS. Unlike the traditional methods, CEST contrasts emerge from the exchangeable protons of drug molecules, and therefore no extrinsic chemical agent is needed for drug imaging. This eliminates the limitations associated with imaging agents used in traditional techniques. Thus, theranostics based on CEST is promising tool for basic and clinical investigations [55].

The development of CEST drug evaluation is possible for drugs that contain slow to intermediate exchanging protons [22, 56, 57]. In the current study, we focused on the assessment of CEST contrasts of 3TC and FTC. Both ARVs are cytidine analogs and possess a hydroxyl proton and an amino proton in the chemical structure. We posit that other NRTIs can be detected using parallel CEST MRI methods as they also contain hydroxyl and amino protons. For example, tenofovir is an adenosine analog that has an amino group and two hydroxyl groups and abacavir (ABC) is a guanosine analog that has an amino group, an amide group and a hydroxyl group. Notably, CEST also has the potential to image other classes of ARVs such as integrase strand transfer inhibitors (INSTIs), non-nucleoside reverse transcriptase inhibitors (NNRTIs) and protease inhibitors provided that have slow to intermediate exchanging protons. For ARVs from these classes, characterization of CEST effects can be completed by structural evaluation and exchange rate calculations [58, 59].

Although we tested the CEST-based brain imaging, the method with a few modifications in the Lorentzian fitting algorithm can be utilized on other tissues such as liver, kidney and spleen. This significantly expands the applications of the CEST-based detection techniques. Moreover, direct *in vivo* imaging of ARVs could enable long term PK and BD studies, which is critical for the development of long-acting injectables of ARVs. It is now well accepted that long-acting ARVs could affect drug adherence and as such reduce viral transmission, prevent new infections, and limit the emergence of viral drug resistance [60–63]. There is an increasing need for personalized ARV regimens to provide efficient treatment while minimizing toxicity and decreasing the risk of viral resistance developing [64–66]. ARV theranostics that measures real-time tissue drug levels will help the design of personalized treatments tailored for individual patients.

A successful bioimaging technique measures the biodistribution of an ARV with sensitivity and specificity. In this study, the relatively high correlations between imaging results and UPLC-MS/MS measurements of 3TC were observed. This showed that CEST imaging is sensitive to drug levels in CNS. Although the current proof-of-concept study successfully measured the biodistribution of 3TC in brain sub-regions *in vivo*, the test limitations are recognized. *First*, only one dosage of 3TC was utilized that was five times higher than the currently used clinical dose. *Second*, mice were treated with LPS to induce neuroinflammation. Such inflammatory responses are more limited in HIV-1 infected patients with ARV-induced undetectable viral loads and the treatments could enhance brain drug penetration. Such technical limitations will be addressed in future research by using CEST methods to evaluate various ARV dose concentrations independently or in

combination. These studies are now being implemented in HIV-1 infected humanized mice who maintain undetectable viral loads with ARV treatment. Such approach will help to determine and improve the sensitivity of the CEST contrasts. The saturation RF power and duration in the current study was selected based on previous *in vivo* CEST studies [42, 67]. RF parameters will be further optimized in the future using ARVs in cells as suggested in [41] to improve sensitivity for *in vivo* environments.

The major challenge for sufficient specificity for *in vivo* ARV measurements is the contaminations by protons from background biomolecules including proteins and metabolites. Additionally, the MT contrasts from semisolid macromolecules and NOE also confound the ARV CEST contrasts [68]. Simple asymmetric *MTR* analysis, usually, fails for *in vivo* CEST data analysis. Thus, more advanced data analysis methods like the Lorentzian line-shape fitting needs be used to improve the analysis outcome[19, 43, 69–72]. This study demonstrated that Lorentzian functions successfully detected 3TC *in vivo* by fitting the amino proton CEST effect. We posit that the specificity of 3TC detection can be further improved by fitting the combined CEST effects of the amino and hydroxyl protons. Based on this idea, we are extending the Lorentzian method to a multiple-peak algorithm that fits CEST effects of different protons simultaneously in an ARV using Lorentzian functions and polynomials. The method can be further expanded to include values from amide and aliphatic nuclear Overhauser effect (NOE) effects. Algorithms are being developed that utilizes unique “CEST score” that is generated from different CEST values representing different protons, amide and NOE of an ARV. These refinements will certainly improve the assay sensitivity and specificity. This method is inspired by previous work[30, 42, 73], and can be used to identify different ARVs used in combined ARV regimens.

In conclusion, we demonstrated that the CEST effects of cytidine analogs (3TC and FTC) can be characterized. These characterized properties can be harnessed for *in vivo* drug detection and quantification using MRI and advanced data analysis algorithms like Lorentzian line-shape fitting. ARV theranostics based on intrinsic CEST effects will advance the field in evaluating the spatial-temporal biodistribution of drugs and in understanding ARV-associated efficacy and toxicity.

Supplementary Material

Refer to Web version on PubMed Central for supplementary material.

Acknowledgements

Authors thank Bhagya Laxmi Dyavar Shetty for technical assistance with drug quantitation by UPLC-MS/MS, and Melissa Mellon and Lirong Xu in MRI core facility for mouse imaging. This study was partially supported by Nebraska Research Initiative, an NIH Center of Biomedical Research Excellence (COBRE) Nebraska Center for Nanomedicine (NCN) (NIH P20GM127200), and an NIH Program Project Grant (NIH P01DA028555).

References:

1. Heaton RK, Clifford DB, Franklin DR Jr., Woods SP, Ake C, Vaida F, et al.HIV-associated neurocognitive disorders persist in the era of potent antiretroviral therapy: CHARTER Study. Neurology2010; 75(23):2087–2096. [PubMed: 21135382]

2. Heaton RK, Marcotte TD, Mindt MR, Sadek J, Moore DJ, Bentley H, et al.The impact of HIV-associated neuropsychological impairment on everyday functioning. J Int Neuropsychol Soc2004; 10(3):317–331. [PubMed: 15147590]

3. Phanuphak N, Gulick RM. HIV treatment and prevention 2019: current standards of care. Curr Opin HIV AIDS2020; 15(1):4–12. [PubMed: 31658110]

4. Ghosn J, Taiwo B, Seedat S, Autran B, Katlama C. HIV. The Lancet2018; 392(10148):685–697.

5. Saylor D, Dickens AM, Sacktor N, Haughey N, Slusher B, Pletnikov M, et al.HIV-associated neurocognitive disorder--pathogenesis and prospects for treatment. Nat Rev Neurol2016; 12(4):234–248. [PubMed: 26965674]

6. Valcour V, Chalermchai T, Sailasuta N, Marovich M, Lerdlum S, Suttichom D, et al.Central nervous system viral invasion and inflammation during acute HIV infection. The Journal of infectious diseases2012; 206(2):275–282. [PubMed: 22551810]

7. Hong S, Banks WA. Role of the immune system in HIV-associated neuroinflammation and neurocognitive implications. Brain, behavior, and immunity2015; 45:1–12.

8. Katuri A, Bryant J, Heredia A, Makar TK. Role of the inflammasomes in HIV-associated neuroinflammation and neurocognitive disorders. Experimental and Molecular Pathology2019; 108:64–72. [PubMed: 30922769]

9. Van den Hof M, Blokhuis C, Cohen S, Scherpbier HJ, Wit F, Pistorius MCM, et al.CNS penetration of ART in HIV-infected children. J Antimicrob Chemother2018; 73(2):484–489. [PubMed: 29126299]

10. Carvalhal A, Gill MJ, Letendre SL, Rachlis A, Bekele T, Raboud J, et al.Central nervous system penetration effectiveness of antiretroviral drugs and neuropsychological impairment in the Ontario HIV Treatment Network Cohort Study. Journal of neurovirology2016; 22(3):349–357. [PubMed: 26572786]

11. Decloedt EH, Rosenkranz B, Maartens G, Joska J. Central nervous system penetration of antiretroviral drugs: pharmacokinetic, pharmacodynamic and pharmacogenomic considerations. Clin Pharmacokinet2015; 54(6):581–598. [PubMed: 25777740]

12. Yilmaz A, Price RW, Gisslen M. Antiretroviral drug treatment of CNS HIV-1 infection. J Antimicrob Chemother2012; 67(2):299–311. [PubMed: 22160207]

13. Nwogu JN, Ma Q, Babalola CP, Adedeji WA, Morse GD, Taiwo B. Pharmacokinetic, Pharmacogenetic, and Other Factors Influencing CNS Penetration of Antiretrovirals. AIDS Res Treat2016; 2016:2587094. [PubMed: 27777797]

14. Asiedu N, Kretchy I, Asampong E. Psycho-behavioral factors associated with neurocognitive performance among people living with HIV on antiretroviral therapy in Accra, Ghana. Afr Health Sci2020; 20(2):487–596. [PubMed: 33163015]

15. Mellgren Å, Eriksson LE, Reinius M, Marrone G, Svedhem V. Longitudinal trends and determinants of patient-reported side effects on ART-a Swedish national registry study. PloS one2020; 15(12):e0242710. [PubMed: 33362248]

16. Treisman GJ, Soudry O. Neuropsychiatric Effects of HIV Antiviral Medications. Drug Saf2016; 39(10):945–957. [PubMed: 27534750]

17. Abers MS, Shandera WX, Kass JS. Neurological and psychiatric adverse effects of antiretroviral drugs. CNS Drugs2014; 28(2):131–145. [PubMed: 24362768]

18. Dou W, Lin CE, Ding H, Shen Y, Dou C, Qian L, et al.Chemical exchange saturation transfer magnetic resonance imaging and its main and potential applications in pre-clinical and clinical studies. Quantitative imaging in medicine and surgery2019; 9(10):1747–1766. [PubMed: 31728316]

19. McMahon MT, Gilad AA. Cellular and Molecular Imaging Using Chemical Exchange Saturation Transfer. Topics in magnetic resonance imaging : TMRI2016; 25(5):197–204. [PubMed: 27748713]

20. Pankowska A, Kochalska K, Lazorczyk A, Dyndor K, Koziol P, Zienczuk B, et al.Chemical exchange saturation transfer (CEST) as a new method of signal obtainment in magnetic resonance molecular imaging in clinical and research practice. Polish journal of radiology2019; 84:e147–e152. [PubMed: 31019609]

21. Sinharay S, Pagel MD. Advances in Magnetic Resonance Imaging Contrast Agents for Biomarker Detection. Annual review of analytical chemistry (Palo Alto, Calif)2016; 9(1):95–115.
22. Wu B, Warnock G, Zaiss M, Lin C, Chen M, Zhou Z, et al.An overview of CEST MRI for non-MR physicists. EJNMMI physics2016; 3(1):19. [PubMed: 27562024]
23. Dreifuss T, Betzer O, Shilo M, Popovtzer A, Motiei M, Popovtzer R. A challenge for theranostics: is the optimal particle for therapy also optimal for diagnostics?Nanoscale2015; 7(37):15175–15184. [PubMed: 26313344]
24. Rahman M, Ahmad MZ, Ahmad J, Firdous J, Ahmad FJ, Mushtaq G, et al.Role of Graphene Nano-Composites in Cancer Therapy: Theranostic Applications, Metabolic Fate and Toxicity Issues. Curr Drug Metab2015; 16(5):397–409. [PubMed: 25429670]
25. Desai NChallenges in development of nanoparticle-based therapeutics. Aaps j2012; 14(2):282–295. [PubMed: 22407288]
26. Kim M, Gillen J, Landman BA, Zhou J, van Zijl PC. Water saturation shift referencing (WASSR) for chemical exchange saturation transfer (CEST) experiments. Magnetic resonance in medicine2009; 61(6):1441–1450. [PubMed: 19358232]
27. Banks WA, Gray AM, Erickson MA, Salameh TS, Damodarasamy M, Sheibani N, et al.Lipopolysaccharide-induced blood-brain barrier disruption: roles of cyclooxygenase, oxidative stress, neuroinflammation, and elements of the neurovascular unit. Journal of neuroinflammation2015; 12(1):223. [PubMed: 26608623]
28. Maggioli E, McArthur S, Mauro C, Kieswich J, Kusters DHM, Reutelingsperger CPM, et al.Estrogen protects the blood-brain barrier from inflammation-induced disruption and increased lymphocyte trafficking. Brain, behavior, and immunity2016; 51:212–222.
29. Haruwaka K, Ikegami A, Tachibana Y, Ohno N, Konishi H, Hashimoto A, et al.Dual microglia effects on blood brain barrier permeability induced by systemic inflammation. Nature communications2019; 10(1):5816.
30. Chen L, Zeng H, Xu X, Yadav NN, Cai S, Puts NA, et al.Investigation of the contribution of total creatine to the CEST Z-spectrum of brain using a knockout mouse model. NMR in biomedicine2017; 30(12).
31. Debnath A, Hariharan H, Nanga RPR, Reddy R, Singh A. Glutamate-Weighted CEST Contrast After Removal of Magnetization Transfer Effect in Human Brain and Rat Brain with Tumor. Molecular imaging and biology2020.
32. Goerke S, Soehngen Y, Deshmane A, Zaiss M, Breitling J, Boyd PS, et al.Relaxation-compensated APT and rNOE CEST-MRI of human brain tumors at 3 T. Magnetic resonance in medicine2019; 82(2):622–632. [PubMed: 30927313]
33. Singh A, Debnath A, Cai K, Bagga P, Haris M, Hariharan H, et al.Evaluating the feasibility of creatine-weighted CEST MRI in human brain at 7 T using a Z-spectral fitting approach. NMR in biomedicine2019; 32(12):e4176. [PubMed: 31608510]
34. Windschuh J, Zaiss M, Meissner JE, Paech D, Radbruch A, Ladd ME, et al.Correction of B1-inhomogeneities for relaxation-compensated CEST imaging at 7 T. NMR in biomedicine2015; 28(5):529–537. [PubMed: 25788155]
35. Zaiss M, Schuppert M, Deshmane A, Herz K, Ehses P, Fullbier L, et al.Chemical exchange saturation transfer MRI contrast in the human brain at 9.4T. NeuroImage2018; 179:144–155. [PubMed: 29894826]
36. Cai K, Singh A, Poptani H, Li W, Yang S, Lu Y, et al.CEST signal at 2ppm (CEST@2ppm) from Z-spectral fitting correlates with creatine distribution in brain tumor. NMR in biomedicine2015; 28(1):1–8. [PubMed: 25295758]
37. Guo D, Zhou T, Arainga M, Palandri D, Gautam N, Bronich T, et al.Creation of a Long-Acting Nanoformulated 2',3'-Dideoxy-3'-Thiacytidine. Journal of acquired immune deficiency syndromes (1999)2017; 74(3):e75–e83. [PubMed: 27559685]
38. Smith N, Bade AN, Soni D, Gautam N, Alnouti Y, Herskovitz J, et al.A long acting nanoformulated lamivudine ProTide. Biomaterials2019; 223:119476. [PubMed: 31525692]
39. Soni D, Bade AN, Gautam N, Herskovitz J, Ibrahim IM, Smith N, et al.Synthesis of a long acting nanoformulated emtricitabine ProTide. Biomaterials2019; 222:119441. [PubMed: 31472458]

40. Nair AB, Jacob S. A simple practice guide for dose conversion between animals and human. J Basic Clin Pharm2016; 7(2):27–31. [PubMed: 27057123]
41. Bagga P, Pickup S, Crescenzi R, Martinez D, Borthakur A, D'Aquilla K, et al.In vivo GluCEST MRI: Reproducibility, background contribution and source of glutamate changes in the MPTP model of Parkinson's disease. Scientific reports2018; 8(1):2883. [PubMed: 29440753]
42. Chen L, Barker PB, Weiss RG, van Zijl PCM, Xu J. Creatine and phosphocreatine mapping of mouse skeletal muscle by a polynomial and Lorentzian line-shape fitting CEST method. Magnetic resonance in medicine2019; 81(1):69–78. [PubMed: 30246265]
43. Zaiss M, Xu J, Goerke S, Khan IS, Singer RJ, Gore JC, et al.Inverse Z-spectrum analysis for spillover-, MT-, and T1 -corrected steady-state pulsed CEST-MRI--application to pH-weighted MRI of acute stroke. NMR in biomedicine2014; 27(3):240–252. [PubMed: 24395553]
44. Zhuang Z, Shen Z, Chen Y, Dai Z, Zhang X, Mao Y, et al.Mapping the Changes of Glutamate Using Glutamate Chemical Exchange Saturation Transfer (GluCEST) Technique in a Traumatic Brain Injury Model: A Longitudinal Pilot Study. ACS Chemical Neuroscience2019; 10(1):649–657. [PubMed: 30346712]
45. Dadfar SM, Roemhild K, Drude NI, von Stillfried S, Knüchel R, Kiessling F, et al.Iron oxide nanoparticles: Diagnostic, therapeutic and theranostic applications. Adv Drug Deliv Rev2019; 138:302–325. [PubMed: 30639256]
46. Lux F, Sancey L, Bianchi A, Crémillieux Y, Roux S, Tillement O. Gadolinium-based nanoparticles for theranostic MRI-radiosensitization. Nanomedicine (Lond)2015; 10(11):1801–1815. [PubMed: 25715316]
47. Zhu L, Zhou Z, Mao H, Yang L. Magnetic nanoparticles for precision oncology: theranostic magnetic iron oxide nanoparticles for image-guided and targeted cancer therapy. Nanomedicine (Lond)2017; 12(1):73–87. [PubMed: 27876448]
48. Bailly C, Cléry PF, Faivre-Chauvet A, Bourgeois M, Guérard F, Haddad F, et al.Immuno-PET for Clinical Theranostic Approaches. International journal of molecular sciences2016; 18(1).
49. Bodet-Milin C, Bailly C, Touchefeu Y, Frampas E, Bourgeois M, Rauscher A, et al.Clinical Results in Medullary Thyroid Carcinoma Suggest High Potential of Pretargeted Immuno-PET for Tumor Imaging and Theranostic Approaches. Front Med (Lausanne)2019; 6:124. [PubMed: 31214593]
50. Lenzo NP, Meyrick D, Turner JH. Review of Gallium-68 PSMA PET/CT Imaging in the Management of Prostate Cancer. Diagnostics (Basel)2018; 8(1).
51. Pruis IJ, van Dongen G, Veldhuijzen van Zanten SEM. The Added Value of Diagnostic and Theranostic PET Imaging for the Treatment of CNS Tumors. International journal of molecular sciences2020; 21(3).
52. Gupta N, Rai DB, Jangid AK, Kulhari H. A Review of Theranostics Applications and Toxicities of Carbon Nanomaterials. Curr Drug Metab2019; 20(6):506–532. [PubMed: 30251600]
53. Bruna Galdorfini C-A, Marina Paiva A, Eloísa Berbel M, Bruna Lallo da S, Nathalia Cristina R, João Augusto O-J, et al.Drug Delivery Using Theranostics: An Overview of its Use, Advantages and Safety Assessment. Current Nanoscience2020; 16(1):3–14.
54. Li M, Sagastume E, Zepeda-Orozco D, Wen H, Graves S, Lee D, et al.Preclinical evaluation of 203/212Pb-based theranostics-dosimetry and renal toxicity.. Journal of Nuclear Medicine2020; 61(supplement 1):289–289.
55. Li Y, Chen H, Xu J, Yadav NN, Chan KW, Luo L, et al.CEST theranostics: label-free MR imaging of anticancer drugs. Oncotarget2016; 7(6):6369–6378. [PubMed: 26837220]
56. Sherry AD, Wu Y. The importance of water exchange rates in the design of responsive agents for MRI. Curr Opin Chem Biol2013; 17(2):167–174. [PubMed: 23333571]
57. Soesbe TC, Wu Y, Dean Sherry A. Advantages of paramagnetic chemical exchange saturation transfer (CEST) complexes having slow to intermediate water exchange properties as responsive MRI agents. NMR in biomedicine2013; 26(7):829–838. [PubMed: 23055299]
58. Dixon WT, Ren J, Lubag AJ, Ratnakar J, Vinogradov E, Hancu I, et al.A concentration-independent method to measure exchange rates in PARACEST agents. Magnetic resonance in medicine2010; 63(3):625–632. [PubMed: 20187174]
59. Sun PZ, Wang Y, Dai Z, Xiao G, Wu R. Quantitative chemical exchange saturation transfer (qCEST) MRI--RF spillover effect-corrected omega plot for simultaneous determination of

labile proton fraction ratio and exchange rate. Contrast Media Mol Imaging2014; 9(4):268–275. [PubMed: 24706610]

60. Dash PK, Gendelman HE, Roy U, Balkundi S, Alnouti Y, Mosley RL, et al.Long-acting nanoformulated antiretroviral therapy elicits potent antiretroviral and neuroprotective responses in HIV-1-infected humanized mice. Aids2012; 26(17):2135–2144. [PubMed: 22824628]
61. Dash PK, Kaminski R, Bella R, Su H, Mathews S, Ahooyi TM, et al.Sequential LASER ART and CRISPR Treatments Eliminate HIV-1 in a Subset of Infected Humanized Mice. Nature communications2019; 10(1):2753.
62. Canetti D, Spagnuolo V. An evaluation of cabotegravir for HIV treatment and prevention. Expert Opin Pharmacother2020:1–12.
63. Flexner C, Owen A, Siccardi M, Swindells S. LONG-ACTING DRUGS AND FORMULATIONS FOR THE TREATMENT AND PREVENTION OF HIV. Int J Antimicrob Agents2020:106220. [PubMed: 33166693]
64. Mu Y, Kodidela S, Wang Y, Kumar S, Cory TJ. The dawn of precision medicine in HIV: state of the art of pharmacotherapy. Expert opinion on pharmacotherapy2018; 19(14):1581–1595. [PubMed: 30234392]
65. Cusato J, Allegra S, Nicolò A, Calcagno A, D'Avolio A. Precision medicine for HIV: where are we?Pharmacogenomics2018; 19(2):145–165. [PubMed: 29202676]
66. Lengauer T, Pfeifer N, Kaiser R. Personalized HIV therapy to control drug resistance. Drug Discovery Today: Technologies2014; 11:57–64. [PubMed: 24847654]
67. Chen L, Wei Z, Cai S, Li Y, Liu G, Lu H, et al.High-resolution creatine mapping of mouse brain at 11.7 T using non-steady-state chemical exchange saturation transfer. NMR in biomedicine2019; 32(11):e4168. [PubMed: 31461196]
68. Pagel MM. The Pursuit of Theranostics with CEST MRI. Theranostics2016; 6(10):1601–1602. [PubMed: 27446493]
69. Kim J, Wu Y, Guo Y, Zheng H, Sun PZ. A review of optimization and quantification techniques for chemical exchange saturation transfer MRI toward sensitive in vivo imaging. Contrast Media Mol Imaging2015; 10(3):163–178. [PubMed: 25641791]
70. Liu G, Song X, Chan KWY, McMahon MT. Nuts and bolts of chemical exchange saturation transfer MRI. NMR in biomedicine2013; 26(7):810–828. [PubMed: 23303716]
71. Liu Y, Kevadiya BD, Herskovitz J, Gendelman HE. Novel HIV Detection by Chemical Exchange Saturation Transfer (CEST). In: 2019 World Molecular Imaging Congress. Montreal, Canada: World Molecular Imaging Society; 2019.
72. Vinogradov E, Sherry AD, Lenkinski RE. CEST: from basic principles to applications, challenges and opportunities. Journal of magnetic resonance (San Diego, Calif : 1997)2013; 229:155–172.
73. Ryoo D, Xu X, Li Y, Tang JA, Zhang J, van Zijl PCM, et al.Detection and Quantification of Hydrogen Peroxide in Aqueous Solutions Using Chemical Exchange Saturation Transfer. Anal Chem2017; 89(14):7758–7764. [PubMed: 28627877]

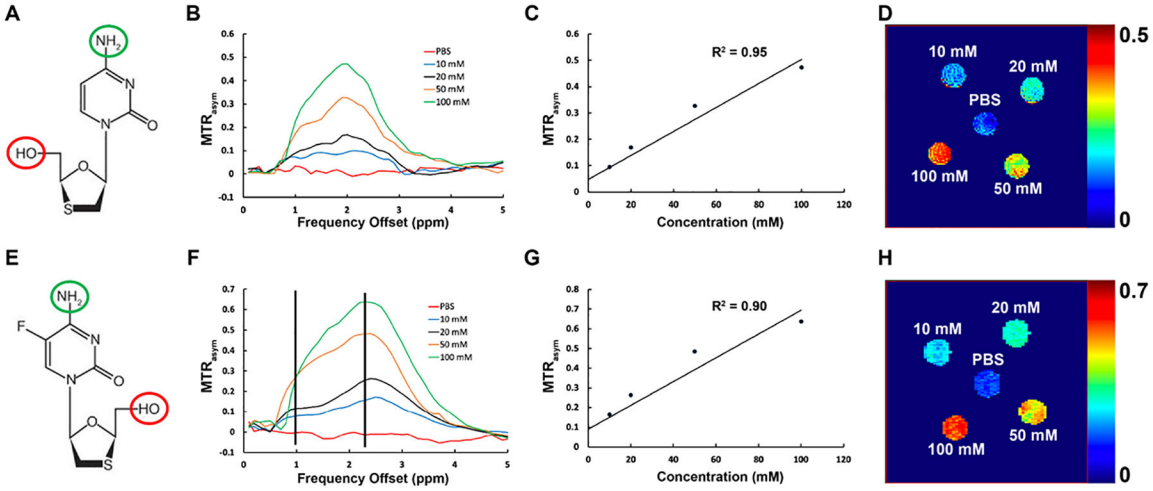

Figure 1.

Chemical exchange saturation transfer (CEST) effects of 3TC and FTC. (**A**) Chemical structure of 3TC. The hydroxyl group is enclosed in red circle, and the amino group is enclosed in blue circle. (**B**) *MTR* plots of 3TC and PBS (control) at 37°C. *MTR* increases at 1 ppm and 2 ppm with the 3TC concentration. PBS did not show CEST effect. (**C**) 3TC amino proton CEST effect (MTR@2ppm) increases linearly with 3TC concentration ($R^2 = 0.95$). (**D**) Pixel-by-pixel heatmaps of 3TC samples. Color intensity increases with 3TC concentration. The color bar for the heatmaps is at the side of the figure represents *MTR* values. (**E**) Chemical structure of FTC. The hydroxyl group is enclosed in red circle, and the amino group is enclosed in blue circle. (**F**) *MTR* plots of FTC and PBS (control) at 37°C. *MTR* increases at 1 ppm and 2 ppm with the FTC concentration. PBS did not show CEST effect. (**G**) FTC amino proton CEST effect (MTR@2ppm) increases linearly with FTC concentration ($R^2 = 0.90$). (**H**) Pixel-by-pixel heatmaps of FTC samples. Color intensity increases with FTC concentration. The color bar for the heatmaps is at the side of the figure represents *MTR* values.

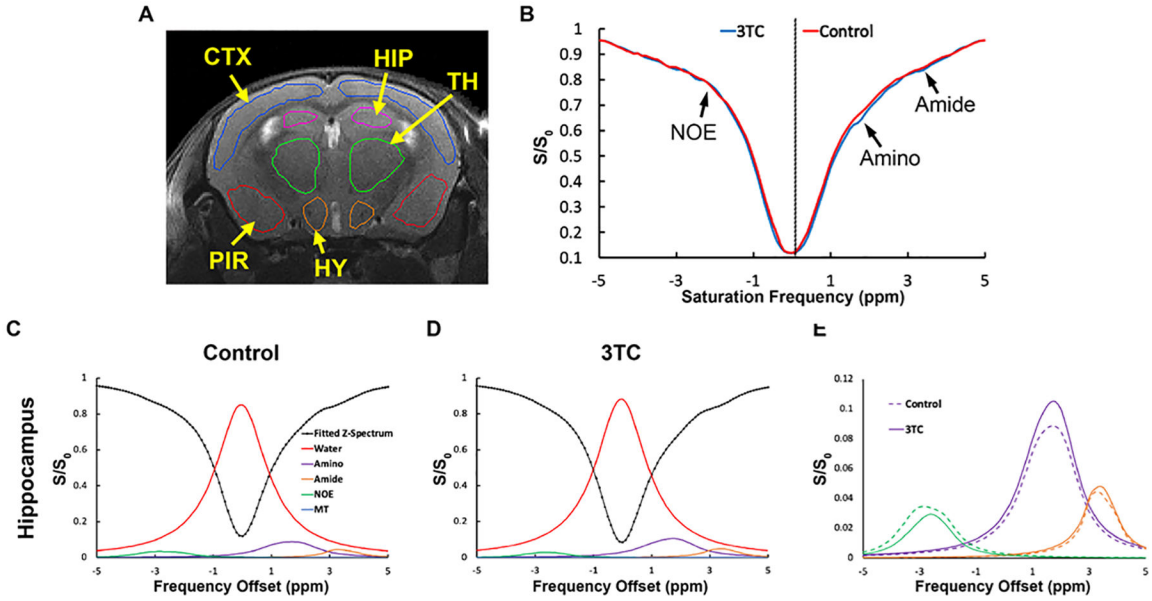

Figure 2.

In vivo chemical exchange saturation transfer (CEST) effects of 3TC. (**A**) Regional CEST effects were measured on hippocampus (HIP), cortex (CTX), piriform cortex (PIR), thalamus (TH) and hypothalamus (HY) (**B**) Representative Z-spectra on HIP of a control and a 3TC-treated mouse. (**C**) and (**D**) Representative fitted five Lorentzian functions of bulk water, aliphatic NOE, MT, amino and amide protons on HIP from a control and a 3TC-treated mouse. The sum of the fitted functions is also shown as fitted Z-spectrum. The Lorentzian functions are shown upside down. (E) The fitted NOE, amino and amide protons are shown for better visualization.

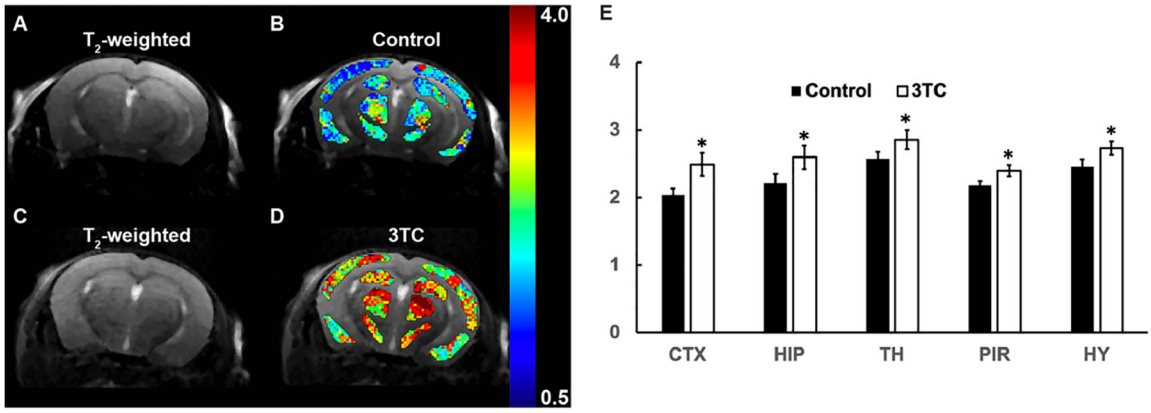

Figure 3.

(**A** and **B**) T_2-weighted image of a control mouse, and pixel-by-pixel Lorentzian line integral heatmaps of fitted amino proton effect superimposed on the respective T_2-weighted image. (**C** and **D**) T_2-weighted image of a 3TC-treated mouse, and pixel-by-pixel Lorentzian line integral heatmaps of fitted amino protons superimposed on the respective T_2-weighted image. (**E**) Group comparisons of fitted integrals of amino proton chemical exchange saturation transfer (CEST) effect. Student's t test (two-tailed) was used to compare *in vivo* CEST imaging results from the control and 3TC groups, *: $p < 0.05$. Data are expressed as mean ± standard error of the mean (SEM); N = 8 (Control) and N = 7 (3TC)

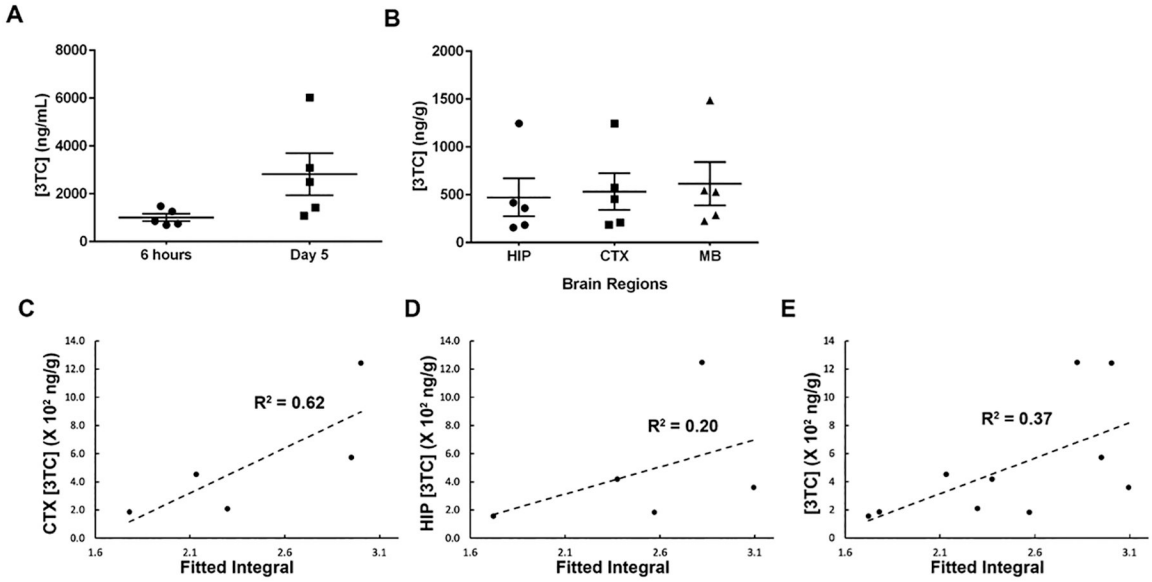

Figure 4.

(**A**) Plasma 3TC levels. (B) 3TC concentrations in hippocampus (HIP), cortex (CTX), and mid-brain (MB) at day 5. For both plasma and brain tissue, 3TC concentrations are expressed as mean ± standard error of the mean (SEM); N = 5/group. (**C**) Correlations of amino proton integrals and tissue 3TC concentrations on CTX. (**D**) Correlations of amino proton integrals and tissue 3TC concentrations on HIP. (**E**) Correlations of amino proton integrals and tissue 3TC concentrations on CTX and HIP combined.